Analyzing the turbulent Planetary Boundary Layer behavior by the synergic use of remote sensing systems: Doppler wind lidar, aerosol elastic lidar and microwave radiometer

Gregori de Arruda Moreira[1,2,3], Juan Luis Guerrero-Rascado[1,2], Jose A. Benavent-Oltra[1,2], Pablo Ortiz-Amezcua[1,2], Roberto Román[1,2,4], Andrés E. Bedoya-Velásquez[1,2,5] Juan Antonio Bravo-Aranda[1,2], Francisco Jose Olmo Reyes[1,2], Eduardo Landulfo[3], Lucas Alados-Arboledas[1,2]

[1]Andalusian Institute for Earth System Research (IISTA-CEAMA), Granada, Spain
[2]Dpt. Applied Physics, University of Granada, Granada, Spain
[3]Institute of Research and Nuclear Energy (IPEN), São Paulo, Brazil
[4]Grupo de Óptica Atmosférica (GOA), Universidad de Valladolid, Valladolid, Spain.
[5]Sciences Faculty, Department of Physics, Universidad Nacional de Colombia, Medellín, Colombia.

Correspondence to: Gregori de Arruda Moreira (gregori.moreira@usp.br)

Abstract

The Planetary Boundary Layer (PBL) is the lowermost region of troposphere and endowed with turbulent characteristics, which can have mechanical and/or thermodynamic origins. Such behavior gives to this layer great importance, mainly in studies about pollutant dispersion and weather forecasting. However, the instruments usually applied in studies about turbulence in the PBL have limitations in spatial resolution (anemometer towers) or temporal resolution (instrumentation onboard aircraft). In this study we propose the synergetic use of remote sensing systems (microwave radiometer [MWR], Doppler lidar [DL] and elastic lidar [EL]) to analyze the turbulent PBL behavior. Furthermore, we show how some meteorological variables such as air temperature, aerosol number density, vertical wind speed, relative humidity and net radiation might influence the turbulent PBL dynamic.The statistical moments of the high frequency distributions of the vertical wind velocity, derived from DL and of the backscattered coefficient derived from EL, are corrected by two methodologies, namely first lag and -2/3 correction. The corrected profiles present small differences when compared against the uncorrected profiles, showing low influence of noise and the viability of the proposed methodology. Two case studies were analyzed in detail, one corresponding to a well-defined PBL and another one corresponding to a situation with presence of a Saharan dust lofted aerosol layer and clouds. In both cases the results provided by the different instruments are complementary, thus the synergistic use of the different systems allow us performing a detailed monitoring of the turbulent PBL behavior, as well as, a better understanding about how the analyzed variables can interfere in this process.

Keywords: Turbulence, Planetary Boundary Layer, Doppler lidar, elastic lidar, microwave radiometer, Earlinet.

1 Introduction

The Planetary Boundary Layer (PBL) is the atmospheric layer directly influenced by the Earth's surface that responds to its changes within time scales around an hour (Stull, 1988). Such layer is located at the lowermost region of troposphere, and is mainly characterized by turbulent processes and a daily evolution cycle. In an ideal situation, instants after sunrise, ground surface temperature increase due to the positive net radiative flux (R_n). This process intensifies the convection, thus, the ascending warm air masses heat the air masses situated in the upper regions of troposphere, originating the Convective Boundary Layer (CBL) or Mixing Layer (ML), which has this name due to a mixing process generated by this turbulent ascending air parcels. Some instants before sunset the gradual reduction of incoming solar irradiance at the Earth's surface causes the decrease of the positive R_n and its change in sign. In this situation, there is a reduction of the convective processes and a weakening of the turbulence. In this process the CBL leads to the development of two layers, namely a stably stratified boundary layer called Stable Boundary Layer (SBL) close to the surface, and the Residual Layer (RL) that contains features from the previous day's ML and is just above the SBL.

Knowledge of the turbulent processes in the CBL is important in diverse studies, mainly for atmospheric modeling and pollutant dispersion, since turbulent mixing can be considered as the primary process by which aerosol particles and other scalars are transported vertically in atmosphere. Because turbulent processes are treated as nondeterministic, they are characterized and described by their statistical properties (high order statistical moments). When applied to atmospheric studies such analysis provide information about the field of turbulent fluctuation, as well as, a description of the mixing process in the PBL (Pal et al., 2010).

Anemometer towers have been widely applied in studies about turbulence (e.g., Kaimal and Gaynor, 1983; van Ulden and Wieringa, 1996), however the limited vertical range of these equipment restrict the analysis to regions close to surface. Aircraft have also been used in atmospheric turbulence studies (e.g., Lenschow et al., 1980; Williams and Hacker, 1992; Lenschow et al., 1994; Albrecht et al., 1995; Stull et al., 1997; Andrews et al., 2004; Vogelmann et al., 2012), nevertheless their short time window limits the analysis. In this scenario, systems with high spatial and temporal resolution and enough range are necessary in order to provide more detailed results along the day throughout the whole thickness of the PBL.

In the last decades, lidar systems have been increasingly applied in this kind of study due to their large vertical range, high data acquisition rate and capability to detect several observed quantities such as vertical wind velocity [Doppler lidar] (e.g. Lenschow et al., 2000; Lothon et al., 2006; O'Connor et al., 2010), water vapor [Raman lidar and DIAL] (e.g. Wulfmeyer, 1999; Kiemle et al., 2007; Wulfmeyer et al., 2010; Turner et al., 2014; Muppa et al., 2015), temperature [rotational Raman lidar] (e.g. Behrendt et al., 2015) and aerosol [elastic lidar] (e.g. Pal et al., 2010; McNicholas et al., 2015). This allows the observation of a wide range of atmospheric processes. For example, Pal et al. (2010) demonstrated how the statistical analyses obtained from high-order moments of elastic lidar can provide information about aerosol plume dynamics in the PBL region. In addition, when different lidar systems operate synergistically, as for example in Engelmann et al. (2008), who combined elastic and Doppler lidar data, it is possible to identify very complex variables such as vertical particle flux. However, this subject requires more exploration, mainly the synergy among lidar and others remote sensing systems, like microwave radiometer. Thus, the combination of information obtained from these instruments can provide a more detailed understanding about the turbulent PBL behavior. Such approach is even more attractive when considering facilities of networks, e. g. European Aerosol Research Lidar NETwork (EARLINET) (Pappalardo et al., 2014), Microwave Radiometer Network (MWRNET) (Rose et al., 2005; Caumont et al., 2016) and ACTRIS CLOUDNET (Illingworth et al., 2007).

Therefore, considering this scenario, in this study we use synergistically the data of three remote sensing systems (Elastic Lidar [EL], Doppler Lidar [DL] and Microwave Radiometer [MWR]) acquired during the SLOPE-I campaign, held at IISTA-CEAMA (Andalusian Institute for Earth System Research, Granada, Spain) from May to August 2016, in order to analyze the turbulent PBL behavior and to improve our comprehension about how each analyzed variable influence the PBL dynamics.

This paper is organized as follows. Description of the experimental site and the equipment setup are presented in Section 2. The methodologies applied are introduced in Section 3. Section 4 presents the results of the analyses using the different methodologies. Finally, conclusions are summarized in Section 5.

2 Experimental site and instrumentation

The SLOPE-I (Sierra nevada Lidar aerOsol Profiling Experiment) campaign was performed from May to September 2016 in South-Eastern Spain in the framework of the European Research Infrastructure for the observation of Aerosol, Clouds, and Trace gases (ACTRIS). The main objective of this campaign was to perform a closure study by comparing remote sensing system retrievals of atmospheric aerosol properties, using remote systems operating at the Andalusian Institute of Earth System Research (IISTA-CEAMA) and in-situ measurements operating at different altitudes in the Northern slope of Sierra Nevada, around 20 km away from IISTA-CEAMA (Bedoya-Velásquez et al., 2018; Román et al., 2018). The IISTA-CEAMA station is part of EARLINET (Pappalardo et al, 2014) since 2005 and at present is an ACTRIS station (http://actris2.nilu.no/). The research facilities are located at Granada, a medium size city in Southeastern Spain (Granada, 37.16°N, 3.61°W, 680 m a.s.l.), surrounded by mountains and with Mediterranean-continental climate conditions that are responsible for cool winters and hot summers. Rain is scarce, especially from late spring to early autumn. Granada is affected by different kind of aerosol particles locally originated and medium-long range transported from Europe, Africa and North America (Lyamani et al., 2006; Guerrero-Rascado et al., 2008, 2009; Titos et al., 2012; Navas-Guzmán et al., 2013; Valenzuela et al., 2014, Ortiz-Amezcua et al, 2014, 2017).

MULHACEN is a biaxial ground-based Raman lidar system operated at IISTA-CEAMA in the frame of EARLINET research network. This system operates with a pulsed Nd:YAG laser, frequency doubled and tripled by Potassium Dideuterium Phosphate crystals, emitting at wavelengths of 355, 532 and 1064 nm with output energies per pulse of 60, 65 and 110 mJ, respectively. MULHACEN operates with three elastic channels: 355, 532 (parallel and perpendicular polarization) and 1064 nm and three Raman-shifted channels: 387 (from N_2), 408 (from H_2O) and 607 nm (from N_2). MULHACEN's overlap is complete at 90% between 520 and 820 m a.g.l. for all the wavelengths, reaching full overlap around 1220 m a.g.l. (Navas-Guzmán et al ., 2011; Guerrero-Rascado et al. 2010). Calibration of the depolarization capabilities is done following Bravo-Aranda et al. (2013). This system was operated with a temporal and spatial resolution of 2 s and 7.5 m, respectively. More details can be found at Guerrero-Rascado et al. (2008, 2009).

The Doppler lidar (Halo Photonics, model Stream Line XR) is also operated at IISTA-CEAMA. This system works in continuous and automatic mode from May 2016. It operates at 1.5 µm with pulse energy and repetition rate of 100 µJ and 15 KHz, respectively. This system record the backscattered signal with 300 gates, being the range gate length 30 m, with the first gate at 60 m. The telescope focus is set to approximately 800 m. For this work the data were collected in stare mode (laser beam is pointed at vertical with respect to the ground surface) with a time resolution of 2 s.

Furthermore, we operated the ground-based passive microwave radiometer (RPG-HATPRO G2, Radiometer Physics GmbH), which is member of the MWRnet [http://cetemps.aquila.infn.it/mwrnet/]. This system operates in automatic and continuous mode at IISTA-CEAMA since November 2011. The microwave radiometer (MWR) measures the sky brightness temperature with a radiometric resolution between 0.3 and 0.4 K root mean square error at 1 s integration time, using direct detection receivers within two bands: K-band (water vapor – frequencies: 22.24 GHz, 23.04 GHz, 23.84 GHz, 25.44 GHz, 26.24 GHz, 27.84 GHz, 31.4 GHz) and V-band (oxygen – frequencies: 51.26 GHz, 52.28 GHz, 53.86 GHz, 54.94 GHz, 56.66 GHz, 57.3 GHz, 58.0 GHz). From these bands is possible to obtain profiles of water vapor and temperature, respectively, by inversion algorithms described in Rose et al. (2005). The range resolution of these profiles vary between 10 and 200 m in the first 2 km and between 200 and 1000 m in the layer between 2 and 10 km (Navas-Guzmán et al., 2014).

The meteorological sensor (HMP60, Vaisala) is used to register the air surface temperature and surface relative humidity, with a temporal resolution of 1 minute. Relative humidity is monitored with an accuracy of ± 3%, and air surface temperature is acquired with an accuracy and precision of 0.6º C and 0.01º C, respectively.

A CM-11 pyranometer manufactured by Kipp & Zonen (Delft, The Netherlands) is also installed in the ground-based station. This equipment measures the shortwave (SW) solar global horizontal irradiance data (305–2800 nm). The CM-11 pyranometer complies with the specifications for the first-class WMO (World Meteorological Organization) classification of this instrument (resolution better than ±5 Wm^{-2}), and the calibration factor stability has been periodically checked against a reference CM-11 pyranometer (Antón et. al, 2012).

3 Methodology

3.1 MWR data analysis

The MWR data are analyzed combining two algorithms, Parcel Method $[PM]$ (Holzworth, 1964) and Temperature Gradient Method $[TGM]$ (Coen, 2014), in order to estimate the PBL Height ($PBLH_{MWR}$) in convective and stable situations, respectively. The different situations are discriminated by comparing the surface potential temperature ($\theta(z_0)$) with the corresponding vertical profile of $\theta(z)$ up to 5 km. Those cases where all the points in the vertical profile have values larger than $\theta(z_0)$ are labeled as stable, and TGM is applied. Otherwise the situation is labeled as unstable and the PM is applied. The vertical profile of $\theta(z)$ is obtained from the vertical profile of T(z) using the following equation (Stull, 2011):

$$\theta(z) = T(z) + 0.0098 * z \quad (1)$$

where $T(z)$ is the temperature profile provided by MWR, z is the height above the sea level, and 0.0098 K/m is the dry adiabatic temperature gradient. A meteorological station co-located with the MWR is used to detect the surface temperature $[T(z_0)]$. In order to reduce the noise, $\theta(z)$ profiles were averaged providing a $PBLH_{MWR}$ value at 30 minutes intervals. This methodology of $PBLH$ detection was selected as the reference due to the results obtained during a performed campaign of comparison between MWR and radiosonde data, where twenty-three radiosondes were launched. High correlations were found between $PBLH$ retrievals provided by both instruments in stable and unstable cases. Further details are given by Moreira et al. (2018a).

3.2 Lidar turbulence analysis

Both lidar systems, DL and EL, gathered data with a temporal resolution of 2 seconds. Then, the data are averaged in 1-hour packages, from which the mean value is extracted $[\bar{q}(z)]$. Such mean value is subtracted from each $q(z,t)$ profile in order to estimate the vertical profile of the fluctuation for the measured variable $[q'(z,t)]$ (i.e. vertical velocity for the DL):

$$q'(z,t) = q(z,t) - \bar{q}(z) \quad (2)$$

Then, from $q'(z,t)$ is possible to obtain the high-order moments (variance ($\boldsymbol{\sigma}^2$), skewness ($\boldsymbol{S}$) and kurtosis ($\boldsymbol{K}$)), as well as, the integral time scale ($\boldsymbol{\tau}$ - which is the time over which the turbulent process are highly correlated to itself) as shown in Table 1. These variables can also be obtained from the following autocovariance function, M_{ij}:

$$M_{ij} = \int_0^{t_f} [q'(z,t)]^i [q'(z, t + t_f)]^j dt \quad (3)$$

where t_f is the final time, i and j indicate the order of autocovariance function.

However, it is necessary to considerer that the acquired real data contain instrumental noise, $\varepsilon(z)$. Therefore, the equation 3 can be rewritten as:

$$M_{ij} = \int_0^{\tau} [q(z,t) + \varepsilon(z,t)]^i [q(z, t + \tau) + \varepsilon(z, t + \tau)]^j dt \quad (4)$$

The autocovariance function of a time series with zero lag results in the sum of the variances of the atmospheric variable and its $\varepsilon(z)$. Nevertheless, atmospheric fluctuations are correlated in time, but the $\varepsilon(z)$ is random and uncorrelated with the atmospheric signal. Consequently, the noise is only associated with lag 0 (Fig. 1). Based on this concept Lenschow et al. (2000) suggested to obtain the corrected autocovariance function, $M_{11}(\rightarrow 0)$, from two methods, namely first lag correction or -2/3 law correction. In the first method, $M_{11}(\rightarrow 0)$ is obtained directly by the subtraction of lag 0, $\Delta M_{11}(0)$, from the autocovariance function, $M_{11}(0)$. In the second method $M_{11}(\rightarrow 0)$ is generated by the extrapolation of $M_{11}(0)$ at firsts nonzero lags back to lag zero (-2/3 law correction). The extrapolation can be performed using the inertial subrange hypothesis, which is described by the following equation (Monin and Yaglom, 1979):

$$M_{11}(\rightarrow 0) = \overline{q'^2(z,t)} + Ct^{2/3} \quad (5)$$

where C represents a parameter of turbulent eddy dissipation rate. The high-order moments and $\boldsymbol{\tau}$ corrections and errors are shown in Table 1 (columns 2 and 3, respectively).

The same procedure of analysis is applied in studies with DL and EL, being the main difference the tracer used by each system, which are the fluctuation of vertical wind speed (w') for DL and aerosol number density (N') for EL. DL provides $w(z,t)$ directly, and therefore the procedure described in Figure 2 can be directly applied. Thus, the two corrections described above are applied separately and finally $\boldsymbol{\tau}$ and high-order moments with and without corrections can be estimated.

On the other hand, the EL does not provide $N(z,t)$ directly. Under some restrictions, it is possible to ignore the particle hygroscopic growth and to assume that the vertical distribution of aerosol type does not changes with time, and to adopt the following relation (Pal et al., 2010):

$$\beta_{par}(z,t) \approx N(z,t)Y(z) \;\Rightarrow \beta'_{par}(z,t) = N'(z,t) \quad (6)$$

where β_{par} and β'_{par} represent the particle backscatter coefficient and its fluctuation, respectively, and Y does not depends on time.

Considering the lidar equation:

$$P_\lambda(z) = P_0 \frac{ct_d}{2} AO(z) \frac{\beta_\lambda(z)}{z^2} e^{-2\int_0^z \alpha_\lambda(z'dz')} \quad (7)$$

where $P_\lambda(z)$ is the signal returned from distance z at time t, z is the distance [m] from the lidar of the volume investigated in the atmosphere, P_0 is the power of the emitted laser pulse, c is the light speed [m/s], t_d is the duration of laser pulse [ns], A is the area [m²] of telescope cross section, $O(z)$ is the overlap function, $\alpha_\lambda(z)$ is the total extinction coefficient (due to atmospheric particles and molecules) [(km)$^{-1}$] at distance z, $\beta_\lambda(z)$ is the total backscatter coefficient (due to atmospheric particles and molecules) [(km·sr)$^{-1}$] at distance z and the subscript λ represents the wavelength. The two path transmittance term related to $\alpha(z)$ is considered as nearly negligible at 1064 nm (Pal et al., 2010). Thus, it is possible to affirm that:

$$RCS_{1064}(z) = P(z)_{1064}.z^2 \cong G.\beta_{1064}(z) \quad (8)$$

and consequently:

$$RCS'_{1064}(z,t) \;\cong \beta'_{1064}(z,t) = \beta'_{par}(z,t) = N'(z,t) \quad (9)$$

where RCS_{1064} and RCS'_{1064} are the range corrected signal and its fluctuation, respectively, G is a constant and the subscripts represent the wavelength.

In this way, Pal et al. (2010) have shown the feasibility of using EL operating at 1064 nm for describing the atmospheric turbulence. In a recent paper Moreira et al. (2018b), have shown that the use of the EL at 532 nm, in spite of the larger attenuation expected at this wavelength due to both aerosol and molecules, provides a description of the turbulence equivalent to that provided by EL operating at 1064 nm. This result is interesting having in mind the more extended use of lidar systems based on laser emission at 532 nm in different coordinated networks. Thus, in EARLINET and LALINET (Latin American LIdar NETwork) around 76% and 45% of the systems include the wavelength of 1064 nm, while 95% of the EARLINET systems and 73% of the LALINET systems operate systems that include the wavelength 532 nm (Guerrero-Rascado et al., 2016). Furthermore, the performance of the lidar systems at 532 nm presents better signal to noise ratio than that encountered at 1064nm. Thus, in this study we use the RCS_{532} for analyzing turbulence using EL, following the procedure described in Figure 3, which is basically the same methodology described earlier for DL.

These three methodologies, together with data of net surface radiation (obtained from pyranometer data) and air temperature (provided by MWR), are used synergistically in order to complement one each other and consequently generate a detailed picture of how each variable influences the turbulent PBL behavior, as it will be demonstrated in subsection 4.2.

4 Results

4.1 Error Analysis

The influence of random error in noisy observations rapidly grows for higher-order moments (i.e., the influence of random noise is much larger for the fourth-order moment than for the third-order moment). Therefore, the first step, in order to ascertain the applied methodology and our data quality, we performed the error treatment of DL data as described in Figure 2.

Figure 4 illustrates the autocovariance function, generates from w', at three different heights. As mentioned before, the lag 0 is contaminated by noise ε, and thus the impact of the noise ε increases together with height, mainly above $PBLH_{MWR}$ (1100 m a.g.l. in our example).

Figure 5-A illustrates the comparison between integral time scale ($\boldsymbol{\tau_{w'}}$) without correction and the two corrections cited in section 3.2. Except for the first height, under the $PBLH_{MWR}$ the profiles practically do not have significant difference, as well as small errors bars. Above $PBLH_{MWR}$ the first lag correction presents some differences in relation the other profiles at around 1350 m.

Figures 5-B and 5-C show the comparison of variance ($\boldsymbol{\sigma^2_{w'}}$) and skewness ($\boldsymbol{S_{w'}}$), respectively, with and without corrections. The profiles corrected by -2/3 law do not present significant differences in comparison to uncorrected profiles. On the other hand, the profiles corrected by the first lag correction have significant differences under the $PBLH_{MWR}$, mainly the $\boldsymbol{\sigma}^2_{w'}$ ($\boldsymbol{S}_{w'}$ only in the first 50 m), and some slight differences are evident above $PBLH_{MWR}$.

For EL we use the same procedure for the correction and error analysis that we apply to the DL data. Figure 6 shows the autocovariance function, obtained from RCS', at three distinct heights. As expected, the increase of height produces the increase of ε, principally above the $PBLH_{MWR}$.

Figures 7-A, 7-B, 7-C and 7-D show the vertical profiles of $\boldsymbol{\tau}_{\boldsymbol{RCS'}}$, $\boldsymbol{\sigma}^2_{RCS'}$, $\boldsymbol{S}_{\boldsymbol{RCS'}}$ and kurtosis ($\boldsymbol{K}_{\boldsymbol{RCS'}}$), respectively, with and without the corrections described in section 3.2. In general, the corrections do not affect the profiles in a significant way, especially in the region below the $PBLH_{MWR}$. Above the $PBLH_{MWR}$ some small differences are noticed, mainly in the first lag correction. The error bars associated to each profile also have low values in all cases. When comparing corrected and uncorrected profiles, the largest differences are observed for the profiles at higher order moments, because of error propagation. $\boldsymbol{K}_{\boldsymbol{RCS'}}$ profile is the more affected by corrections, so the kurtosis profile after the first lag correction shows the largest difference with uncorrected profile.

Since the first lag and 2/3 corrections do not have a significant impact within the PBL region, we adopted the first lag correction in order to be more careful during the comparison.

4.2 Case studies

In this section we present two study cases, in order to show how the synergy of methodologies described in section 3 can provide a detailed description about the turbulent PBL behavior. The first case represents a typical day with a clear sky situation. The second case corresponds to a more complex situation, where there is presence of clouds and Saharan mineral dust layers.

4.2.1 Case study I: clear sky situation

In this case study we use measurements gathered with DL, MWR and pyranometer during 24 hours. The EL was operated under operator-supervised mode between 08:20 to 18:00 UTC.

Figure 8 (A) shows the integral time scale obtained from DL data ($\boldsymbol{\tau}_{\boldsymbol{w'}}$). The gray areas represents the region where $\boldsymbol{\tau}_{\boldsymbol{w'}}$ is lower than the acquisition time of DL and, therefore, for this region it is not possible to analyze turbulent processes. However, the gray area is located almost entirely above the $PBLH_{MWR}$ (white stars). Thus, the DL acquisition time allows us to observe the turbulence throughout the whole PBL. The gray areas, as well as, the black lines (air temperature), have the same meaning in Figures 8-B and 8-C.

$\boldsymbol{\sigma}^2_{\mathbf{w'}}$ has low values during the entire period of SBL (Figure 8-B). Nevertheless, as air temperature begins to increase (around 07:00 UTC), $\boldsymbol{\sigma}^2_{\mathbf{w'}}$ increases together, as well as, $PBLH_{MWR}$. $\boldsymbol{\sigma}^2_{\mathbf{w'}}$ reaches its maximum values in the middle of the day, when we also observe the maximum values of air temperature and $PBLH_{MWR}$. This process is in agreement with the behavior of skewness of w' ($\mathbf{S}_{\mathbf{w'}}$) shown in Figure 8-C. $\mathbf{S}_{\mathbf{w'}}$ is directly associated with the direction of turbulent movements. Thus, positive values correspond with a surface-heating-driven boundary layer, while negative ones are associated to cloud-top long-wave radiative cooling. If $\mathbf{S}_{\mathbf{w'}}$ is positive, both $\boldsymbol{\sigma}^2_{\mathbf{w'}}$ and TKE (Turbulent Kinetic Energy) are being transported upwards and consequently, the red regions in Figure 13-C represent positive values of $\mathbf{S}_{\mathbf{w'}}$ and the blue regions refer to negative ones. During the stable period, there is predominance of low values of $\mathbf{S}_{\mathbf{w'}}$. Nevertheless, as air temperature increases (transition from stable to unstable period), $\mathbf{S}_{\mathbf{w'}}$ values begin to become positive and increase with the ascent of the $PBLH_{MWR}$ (CBL). Air temperature begins to decrease around 18:00 UTC, causing the reduction of $\mathbf{S}_{\mathbf{w'}}$. In this moment the transition from unstable to stable period occurs and, therefore, the reduction in $PBLH_{MWR}$ is due to the $SBLH$ detection.

Figure 8-D shows the values of net surface radiation (R_n) that are estimated from solar global irradiance values using the seasonal model described in Alados et al. (2003). The negative values of R_n are concentrated in the stable region. R_n begins to increase around 06:00 UTC and reaches its maximum in the middle of the day. Comparing figures 8-C and 8-D, we can observe similarity among the behavior of $\mathbf{S}_{\mathbf{w'}}$, R_n and surface air temperature, because these variables increase and decrease together, as expected.

The increase of R_n causes the rise of surface air temperature, which contributes to the positive latent heat flux from the surface ($\mathbf{S}_{\mathbf{w'}}$) and, consequently, the growth of the $PBLH_{MWR}$ (CBL). $\mathrm{R_n}$ begins to decrease certain time before the other variables, but the intense reduction of air temperature and decrease of $\mathbf{S}_{\mathbf{w'}}$ and $SBLH$ detection occurs when R_n becomes negative again, although there can still be a positive sensible heat flux, what is characteristic of early evening in urban regions due to the release of the ground heat flux at that time.

Figure 8-E presents the values of surface air temperature and surface relative humidity (RH). Air surface temperature is directly related with R_n and $\mathbf{S}_{\mathbf{w'}}$ values, as aforementioned and expected. On the other hand, RH is inversely correlated with temperature and, thus, with the rest of variables, due to the relative constancy of the water vapor mixing ratio characteristic of our site during the study

Figure 9 shows the RCS_{532} profile obtained from 08:00 to 18:00 UTC and the well-defined $PBLH_{MWR}$ (pink stars). At the beginning of the measurement period (08:20 to 10:00 UTC) it is possible to observe the presence of a thin residual layer (around 2000 m a.s.l.), and later from 13:00 to 18:00 UTC it is evident a lofted aerosol layer. The period between 13:00 and 14:00 UTC has been selected to be analyzed. Figure 10-A presents the profiles of molecular ($\beta_{Molecular}$) and aerosol ($\beta_{Aerosol}$) backscatter coefficients at 532 nm. Although β_{532} is composed by $\beta_{Molecular}$ and $\beta_{Aerosol}$, it is possible to observe the predominance of $\beta_{Aerosol}$ in the region below of the $PBLH_{MWR}$, as demonstrated in figure 10-B by the β_{Ratio} profile. Similar results were demonstrated by Moreira et al. (2018b), therefore reinforcing the viability of the use of this wavelength in studies about turbulence. Figure 11 presents the statistical moments generated from RCS', which were obtained from 13:00 and 14:00 UTC. The maximum for the variance of RCS can be used as indicator of $PBLH$ $(PBLH_{Elastic})$ (Moreira et al., 2015). Thus, the red line in all graphics represent the $PBLH_{Elastic}$ (2200 m a.s.l.) and the blue one the average value of $PBLH_{MWR}$ (2250 m a.s.l.), both obtained between 13 and 14 UTC.

Due to well-defined PBL, $PBLH_{Elastic}$ and $PBLH_{MWR}$ do not have significant differences (50 m). $\boldsymbol{\sigma}^2_{RCS'}$ has small values below the $PBLH$. Above $PBLH_{Elastic}$ the values of $\boldsymbol{\sigma}^2_{RCS'}$ decrease slowly due to location of the lofted aerosol around 2500 m. However, above this aerosol layer the value of $\boldsymbol{\sigma}^2_{RCS'}$ is reduced to zero, indicating the extreme decreasing in aerosol concentration in the free troposphere. The integral time scale obtained from RCS' ($\boldsymbol{\tau}_{\boldsymbol{RCS'}}$) has values higher than EL time acquisition throughout the CBL, evidencing the feasibility for studying turbulence using this elastic lidar configuration. The skewness values obtained from RCS' ($\boldsymbol{S}_{\boldsymbol{RCS'}}$) give us information about aerosol motion. The positive values of $\boldsymbol{S}_{\boldsymbol{RCS'}}$ observed in the lowest part of profile and above the $PBLH_{Elastic}$ represents the updrafts aerosol layers. The negative values of $\boldsymbol{S}_{\boldsymbol{RCS'}}$ indicates the region with low aerosol concentration due to clean air coming from free troposphere (FT). This movement of ascension of aerosol layers and descent of clean air with zero value of $\boldsymbol{S}_{\boldsymbol{RCS'}}$ is characteristic of growing PBL and was also detected by Pal et al. (2010) and McNicholas et al. (2014). The kurtosis of RCS' ($\boldsymbol{K}_{\boldsymbol{RCS'}}$) determines the level of mixing at different heights. There are values of $\boldsymbol{K}_{\boldsymbol{RCS'}}$ larger than 3 in the lowest part of profile and around 2500 m, showing a peaked distribution in this region. On other hand, values of $\boldsymbol{K}_{\boldsymbol{RCS'}}$ lower than 3 are observed close to the $PBLH_{Elastic}$, therefore this region has a well-mixed CBL regime. Pal et al. (2010) and McNicholas et al. (2014) also detected this feature in the region nearby the $PBLH$.

The results provided by DL, pyranometer and MWR data agree with the results observed in Figure 10. In the same way, the analysis of high order moments of RCS' fully agree with the information in Figure 8. Thus, the large values of $\boldsymbol{S}_{\boldsymbol{RCS'}}$ and $\boldsymbol{K}_{\boldsymbol{RCS'}}$ detected around 2500 m a.s.l, where we can see a lofted aerosol layer, suggest the ascent of an aerosol layer and presence of a peaked distribution, respectively.

4.2.2 Case study: dusty and cloudy scenario

In this case study measurements with DL, MWR and pyranometer expand during 24 hours, while EL data are collected from 09:00 to 16:00 UTC.

Figure 12-A shows $\boldsymbol{\tau}_{\boldsymbol{w'}}$, where the black lines and gray area has the same meaning mentioned earlier. Outside the period 13:00 to 17:00 UTC, the grey area is situated completely above the $PBLH_{MWR}$ (white stars), thus DL time acquisition is enough to perform studies about turbulence in this case.

$\boldsymbol{\sigma}^2_{w'}$ has values close to zero during all the stable period (Figure 12-B). However, when air temperature and $PBLH_{MWR}$ begins to increase (around 06:00 UTC), $\boldsymbol{\sigma}^2_{w'}$ also increases and reaches its maximum in the middle of the day. In the late afternoon, as air temperature and $PBLH_{MWR}$ decrease, the values of $\boldsymbol{\sigma}^2_{w'}$ decrease gradually, until reach the minimum value associated to the SBL. Figure 12-C shows the profiles of $\boldsymbol{S}_{\boldsymbol{w'}}$. In the same way of the previous case study, the behavior of $\boldsymbol{S}_{\boldsymbol{w'}}$ is directly related to the air temperature pattern (increasing and decreasing together) and causing the growth and reduction of $PBLH_{MWR}$. The main features of this case are: the low values of $\boldsymbol{S}_{\boldsymbol{w'}}$, the **s**low increase and ascension of positive $\boldsymbol{S}_{\boldsymbol{w'}}$ values and the predominance of negative $\boldsymbol{S}_{\boldsymbol{w'}}$ values from 12:00 to 13:00 UTC. The first two features are likely due to the presence of the intense Saharan dust layer (Figure 13), which reduces the transmission of solar irradiance, and consequently the absorption of solar irradiance at the surface, generating weak convective process. From Figure 13 we can observe the presence of clouds from 12:00 to 14:00 UTC. This justifies the intense negative values of $\boldsymbol{S}_{\boldsymbol{w'}}$ observed in this period, because, as mentioned before, $\boldsymbol{S_{w'}}$ is directly associated with direction of turbulent movements that during this period is associated to cloud-top long-wave radiative cooling, due to the presence of clouds (Ansmann et al., 2010).

The influence of Saharan dust layer can also be evidenced on the R_n pattern (Figure 12-D), which maintains negative values until 12:00 UTC and reaches a low maximum value (around 200 W/m²). Air surface temperature and RH (Figure 12-E) present the same correlation and anti-correlation (respectively) observed in the earlier case study, where the maximum of air surface temperature and the minimum of RH are detected in coincidence with the maximum daily value of $PBLH_{MWR}$.

As mentioned before, Figure 13 shows the RCS profile obtained from 09:00 to 16:00 UTC in a complex situation, with presence of decoupled dust layer (around 3800 m a.s.l.) from 09:00 and 12:00 and clouds (around 3500 m a.s.l.) from 11:00 to 16:00 UTC. The pink stars represent $PBLH_{MWR}$. Figure 14-A presents the $\beta_{Molecular}$ and $\beta_{Aerosol}$ profiles, similarly to Figure 10-A. It is evident the predominance of $\beta_{Aerosol}$ in the region below $PBLH_{MWR}$, as demonstrated by β_{Ratio} profile in figure 14-B. However due to presence of dust layer this dominance of $\beta_{Aerosol}$ is extended to approximately 4500 m a.s.l. Therefore the methodology proposed by Moreira et al. (2018b), based on considerations of Pal et al. (2010), can be applied.

Figure 15 illustrates the statistical moments of RCS' obtained from 11:00 to 12:00 UTC. The $\boldsymbol{\sigma}^2_{RCS'}$ profile presents several peaks due to the presence of distinct aerosol sublayers. The first peak is coincident with the value of $PBLH_{MWR}$. The value of $PBLH_{elastic}$, is coincident with the base of the dust layer. This difficulty to detect the $PBLH$ in presence of several aerosol layers is inherent to the variance method (Kovalev and Eichinger, 2004). The values of $\boldsymbol{\tau_{RCS'}}$ are higher than EL acquisition time all along the PBL, evidencing the feasibility of EL time acquisition for studying the turbulence of PBL in this case. The $\boldsymbol{S_{RCS'}}$ profile has several positive values, due to the large number of aerosol sublayers that are present. The characteristic inflection point of $\boldsymbol{S_{RCS'}}$ is observed in coincidence with the $PBLH_{MWR}$, that confirming the agreement between this point and the $PBLH$. $\boldsymbol{K_{RCS'}}$ has predominantly values lower than 3 below 2500 m, thus shown how this region is well mixed as can see in Figure 13. Values of $\boldsymbol{K_{RCS'}}$ larger than 3 are observed in the highest part of profile, where the dust layer is located.

Figure 16 shows the RCS' high-order moments obtained from 12:00 and 13:00 in presence of cloud cover. The method based on maximum of $\boldsymbol{\sigma}^2_{RCS'}$ locates the $PBLH_{Elastic}$ at the cloud base, due to the high variance of RCS' generated by the clouds. $\boldsymbol{\tau_{RCS'}}$ presents values larger than EL time acquisition, therefore this configuration enable us to study turbulence by EL analyses. $\boldsymbol{S_{RCS'}}$ has few peaks, due to the mixing between CBL and dust layer, generating a more homogenous layer. The highest values of $\boldsymbol{S_{RCS'}}$ are observed in regions where there are clouds, and the negative ones (between 3500 and 4000 m) occur due to presence of air from FT between the two aerosol layers (Figure 13). The inflection point of $\boldsymbol{S_{RCS'}}$ profile is observed in $PBLH_{MWR}$ region. $\boldsymbol{K_{RCS'}}$ profile has low values in most of the PBL, demonstrating the high level of mixing during this period, where dust layer and PBL are combined. The higher values of $\boldsymbol{K_{RCS'}}$ are observed in the region of clouds.

5 Conclusions

In this paper we analyze the turbulent PBL behavior and how each detected variable can influence it. Such observations were made from the synergy of three different types of remote sensing systems (DL, EL and MWR) and surface sensors during SLOPE-I campaign. We applied two kind of corrections to the lidar data: first lag and -2/3 corrections. The corrected DL statistical moments showed little variation with respect to the uncorrected profiles, denoting a rather low influence of the noise. The statistical moments obtained from EL also showed a small variation after correction when compared with the uncorrected profiles, except for $\mathrm{K}_{\mathrm{RCS}'}$, that is more affected by noise. The small changes in the profiles after the corrections, specially inside the PBL, evidence the feasibility of the applied methodology for monitoring the turbulence in the PBL. Nevertheless, all profiles are corrected by first lag correction, which is more restrictive during the comparison, in order to be cautious.

The case studies present two kind of situations: well-defined PBL and a more complex situation with the presence of Saharan dust layer and some clouds. $\sigma_{w'}^2$ and $S_{w'}$ showed a good agreement with the behavior of the air temperature, R_n and $PBLH_{MWR}$ in both situations, highlighting the feasibility in different atmospheric conditions.

The synergic use of remote sensing systems shows how the results provided by the different instruments can complement one each other. Thus, it is possible to observe the direct relationship among PBL growth, $S_{w'}$, $\sigma_{w'}^2$, $\sigma_{RCS'}^2$ and R_n values. In addition, $S_{RCS'}$ and $K_{RCS'}$ provide a good description about aerosol dynamic. The combination of these results gives us a detailed description about PBL dynamic and its structure.

Therefore, this study shows the feasibility of the described methodology based on remote sensing systems for studying the turbulence. The feasibility of using the analyses of high order moments of the RCS collected at 532nm at a temporal resolution of 2 s for the characterization of the atmospheric turbulence in the PBL offers the possibility for using this procedure in networks such as EARLINET or LALINET with a reasonable additional effort.

Acknowledgements

This work was supported by the Andalusia Regional Government through project P12-RNM-2409, by the Spanish Agencia Estatal de Investigación, AEI, through projects CGL2016-81092-R and CGL2017-90884-REDT. We acknowledge the financial support by the European Union's Horizon 2020 research and innovation program through project ACTRIS-2 (grant agreement No 654109). The authors thankfully acknowledge the FEDER program for the instrumentation used in this work and the University of Granada that supported this study through the Excellence Units Program and "Plan Propio. Programa 9 Convocatoria 2013".

References

Alados, I., Foyo-Moreno, I., Olmo, F. J., Alados-Arboledas, L. Relationship between net radiation and solar radiation for semi-arid shrub-land. Agr. Forest Meteorol., 116, 221-227, 2003.

Albrecht, B. A., Bretherton, C. S., Johnson, D., Scubert, W. H., and Frisch, A. S.: The Atlantic stratocumulus transition experiment—ASTEX, Bull. Am. Meteorol. Soc., 76, 889–904, 1995.

Andrews, E., Sheridan, P. J. , Ogren, J. A., and Ferrare, R.: In situ aerosol profiles over the Southern Great Plains cloud and radiation test bed site: 1. Aerosol optical properties, J. Geophys. Res., 109, D06208, doi:10.1029/2003JD004025, 2004.

Ansmann, A., Fruntke, J., Engelmann, R. Updraft and downdraft characterization with Doppler lidar: cloud-free versus cumuli-topped mixed layer. Atmos. Chem. Phys., 10, 7845-7858, 2010.

Antón, M., Valenzuela, A., Cazorla, A., Gil, J. E., Gálvez-Fernández, J., Lyamani, H., Foyo-Moreno, I., Olmo, F. J., Alados-Arboledas, L. Global and diffuse shortwave irradiance during a strong desert dust episode at Granada (Spain). Atmos. Res., 118, 232 – 239, 2012.

Bedoya-Velásquez, A. E., Navas-Guzmán, F., Granados-Muñoz, M. J., Titos, G., Román, R., Casquero-Vera, J. A., Ortiz-Amezcua, P., Benavent-Oltra, J. A., Moreira, G. de A., Montilla-Rosero, E., Ortiz, C. D. H., Artiñano, Coz, E., Alados-Arboledas, L., Guerrero-Rascado, J. L. Hygroscopic growth study in the framework of EARLINET during the SLOPE I campaign: synergy of remote sensing and in-situ instrumentation. Atmos. Chem. Phys., 18, 7001-7017, 2017.

Behrendt, A., Wulfmeyer, V., Hammann, E., Muppa, S. K., Pal, S.: Profiles of second- to fourth-order moments of turbulent temperature fluctuations in the convective boundary layer : first measurements with rotational Raman lidar. Atmos. Chem. Phys., 15, 5485‑5500. https://doi.org/10.5194/acp-15-5485-2015, 2015.

Bravo-Aranda, J. A., Navas-Guzmán, F., Guerrero-Rascado, J. L., Pérez-Ramírez, D., Granados-Muñoz, M. J., Alados-Arboledas, L. Analysis of lidar depolarization calibration procedure and application to the atmospheric aerosol characterization. Int. J. Remote Sens., 34 (9-10), pp. 3543-3560, 2013.

Caumont, O., Cimini, D., Löhnert, U., Alados-Arboledas, L., Bleisch, R., Buffa, F., Ferrario, M.E., Haefele, A., Huet, T., Madonna, F., Pace, G. Assimilation of humidity and temperature observations retrieved from ground-based microwave radiometers into a convective-scale NWP model. Q. J. Roy. Meteor. Soc., 142 (700), pp. 2692-2704, 2016.

Engelmann, R.; Wandinger, U.; Ansmann, A.; Müller, D.; Žeromskis, E.; Althausen, D.; Wehner, B. Lidar Observations of the Vertical Aerosol Flux in the Planetary Boundary Layer. J. Atmos. Ocean. Tech., v. 25, n. 8, p. 1296‑1306, 2008.

Guerrero-Rascado, J.L., Ruiz, B., Alados-Arboledas, L. Multi-spectral lidar characterization of the vertical structure of Saharan dust aerosol over Southern Spain. Atmos. Environ., 42, 2668-2681, 2008.

Guerrero-Rascado, J.L., Olmo, F.J., Avilés-Rodríguez, I., Navas-Guzmán, F., Pérez-Ramírez, D., Lyamani, H., Alados-Arboledas, L.: Extreme Saharan dust event over the southern Iberian Peninsula in September 2007: Active and passive remote sensing from surface and satellite. Atmos. Chem. Phys., 9, 21, 8453-8469, 2009.

Guerrero-Rascado, J. L., Costa, M. J., Bortoli, D., Silva, A. M., Lyamani, H., Alados-Arboledas, L. Infrared lidar overlap function: an experimental determination, Opt. Express, 18, 20350-20359, 2010

Guerrero-Rascado, J. L., Landulfo, E., Antuña, J. C., Barbosa, H. M. J., Barja, B., Bastidas, A. E., Bedoya, A. E., da Costa, R. F., Estevan, R., Forno, R. N., Gouveia, D. A., Jimenez, C., Larroza, E. G., Lopes, F. J. S., Montilla-Rosero, E., Moreira, G. A., Nakaema, W. M., Nisperuza, D., Alegria, D., Múnera, M., Otero, L., Papandrea, S., Pawelko, E., Quel, E. J., Ristori, P., Rodrigues, P. F., Salvador, J., Sánchez, M. F., and Silva, A.: Latin American Lidar Network (LALINET) for aerosol research: diagnosis on network instrumentation, J. Atmos. Sol.-Terr. Phy., 138–139, 112–120, 2016.

Illingworth, A. J., Hogan, R. J. O' Connor, E. J. Bouniol, D. Brooks, M. E. Delanoe, J. Donovan, D. P. Eastment, J. D. Gaussiat, N. Goddard, J. W. F. Haeffelin, M. Klein Baltink, H. Krasnov, O. A. Pelon, J. Piriou, J.-M. Protat, A. Russchenberg, H. W. J. Seifert, A. Tompkins, A. M. Van Zadelhoff, G.-J. Vinit, F. Willen, U. Wilson, D. R. and Wrench, C . L.: CLOUDNET: Continuous Evaluation of Cloud Profiles in Seven Operational Models using Ground-Based Observations. Bull. Am. Meteorol. Soc., 88, 883-898, doi:10.1175/BAMS-88-6-883, 2007.

Kaimal, J. C., and Gaynor, J. E.: The Boulder Atmospheric Observatory, J. Clim. Appl. Meteorol., 22, 863–880, 1983.

Kiemle, C., Brewer, W. A., Ehret, G., Hardesty, R. M., Fix, A., Senff, C., Wirth, M., Poberaj, G., and LeMone, M. A.: Latent heat flux profiles from collocated airborne water vapor and wind lidars during IHOP 2002, J. Atmos. Ocean. Tech., 24, 627–639, 2007.

Kovalev, V.A., Eichinger, W.E., Elastic Lidar, Wiley 2004.

Lenschow, D. H., Wyngaard, J. C., and Pennell, W. T.: Mean-field and second-moment budgets in a baroclinic convective boundary layer, J. Atmos. Sci., 37, 1313–1326, 1980.

Lenschow, D. H., Mann, J., and Kristensen, L.: How long is long enough when measuring fluxes and other turbulence statistics?, J. Atmos. Oceanic Technol., 11, 661–673, 1994.

Lenschow, D. H., Wulfmeyer, V. and Senff, C.: Measuring second- through fourth-order moments in noisy data, J. Atmos. Oceanic Technol., 17, 1330–1347, 2000.

Lenschow, D. H., Lothon, M., Mayor, S. D., Sullivan, P. P., and Canut, G.: A comparison of higher-order vertical velocity moments in the convective boundary layer from lidar with in situ measurements and large-eddy simulation, Bound-Lay. Meteorol., 143, 107–123, doi:10.1007/s10546-011-9615-3., 2012.

Lothon, M., Lenschow, D. H., and Mayor, S. D.: Coherence and scale of vertical velocity in the convective boundary layer from a Doppler lidar, Bound.-Lay. Meteorol., 121, 521–536, 2006.

Lyamani, H., Olmo, F. J., Alcántara, A., and Alados-Arboledas, L.: Atmospheric aerosols during the 2003 heat wave in southeastern Spain I: Spectral optical depth, Atmos. Environ., 40, 6453–6464, 2006

McNicholas, C., Turner, D. D. Characterizing the convective boundary layer turbulence with a High Spectral Resolution Lidar. J. Geophys Res-Atmos., v. 119, p. 910‑927, 2014.

Muppa, K.S., Behrendt, A., Späth, F., Wulfmeyer, V., Metzendorf, S., Riede, A.: Turbulent humidity fluctuations in the convective boundary layer: Cases studies using water vapour differential absorption lidar measurements. Bound-Lay. Meteorol., 158, 43-66, DOI 10.1007/s10546-015-0078-9, 2014.

Monin, A. S., Yaglom, A. M. Statistical Fluid Mechanics, Vol. 2. MIT Press, 874 pp, 1979.

Moreira, G. de A., Marques, M. T. A., Nakaema, W., Moreira, A. C. de C. A., Landulfo, E. Planetary boundary height estimations from Doppler wind lidar measurements, radiosonde and hysplit model comparisom. Óptica Pura y Aplicada, 48, 179-183, 2015

Moreira, G. de A., Guerrero-Rascado, J. L., Bravo-Aranda, J. A., Benavent-Oltra, Ortiz-Amezcua, P., Róman, R., Bedoya-Velásquez, A., Landulfo, E., Alados-Arboledas, L. Study of the planetary boundary layer by microwave radiometer, elastic lidar and Doppler lidar estimations in Southern Iberian Peninsula. Atmos. Res., 213, 185-195, 2018a.

Moreira, G. de A., Lopes, F. J. S., Guerrero-Rascado, J. L., Landulfo, E., Alados-Arboledas, L. Analyzing turbulence in Planetary Boundary Layer from multiwavelenght lidar system: impact of wavelength choice. Opt. Express. Under review, 2018b.

Navas Guzmán, F., Guerrero Rascado, J. L., and Alados Arboledas, L.: Retrieval of the lidar overlap function using Raman signals, Óptica Pura y Aplicada, 44, 71–75, 2011.

Navas-Guzmán, F., Bravo-Aranda, J.A., Guerrero-Rascado, J.L, Granados-Muñoz, M.J, and Alados-Arboledas, L.: Statistical analysis of aerosol optical properties retrieved by Raman lidar over Southeastern Spain. Tellus B, 65, 21234, 2013.

Navas-Guzmán, F., Fernández-Gálvez, J., Granados-Muñoz, M.J, Guerrero-Rascado, J.L., Bravo-Aranda, J.A., and Alados-Arboledas, L.: Tropospheric water vapor and relative humidity profiles from lidar and microwave radiometry. Atmos. Meas. Tech., 7, 1201-1211, 2104.

O'Connor, E. J., Illingworth, A. J., Brooks, I. M., Westbrook, C. D., Hogan, R. J., Davies, F., Brooks, B. J.: A method for estimating the turbulent kinetic energy dissipation rate from a vertically-pointing Doppler lidar, and independent evaluation from balloon-borne in-situ measurements. J. Atmos. Ocean. Tech., v. 27, n. 10, 1652-1664, 2010.

Ortiz-Amezcua, P., Guerrero-Rascado, J.L., Granados-Muñoz, M.J., Bravo-Aranda, J. A., Alados-Arboledas, L. Characterization of atmospheric aerosols for a long range transport of biomass burning particles from canadian forest fires over the southern iberian peninsula in july 2013. Optica Pura y Aplicada, 47 (1), pp. 43-49, 2014.

Ortiz-Amezcua, P., Luis Guerrero-Rascado, J., Granados-Munõz, M.J., Benavent-Oltra, J.A., Böckmann, C., Samaras, S., Stachlewska, I.S., Janicka, L., Baars, H., Bohlmann, S., Alados-Arboledas, L. Microphysical characterization of long-range transported biomass burning particles from North America at three EARLINET stations. Atmos. Chem. Phys., 17 (9), pp. 5931-5946, 2017.

Pal, S.; Behrendt, a.; Wulfmeyer, V. Elastic-backscatter-lidar-based characterization of the convective boundary layer and investigation of related statistics. Ann. Geophys., v. 28, n. 3, p. 825‑847, 2010.

Pappalardo, G., Amodeo, A., Apituley, A., Comeron, A., Freudenthaler, V., Linné, H., Ansmann, A., Bösenberg, J., D'Amico, G., Mattis, I., Mona, L., Wandinger, U., Amiridis, V., Alados-Arboledas, L., Nicolae, D., and Wiegner, M.: EARLINET: towards an advanced sustainable European aerosol lidar network. Atmos. Meas. Tech., 7, 2389-2409, doi:10.5194/amt-7-2389-2014, 2014.

Román, R., Benavent-Oltra, J. A., Casquero-Vera, J. A., Lopatin, A., Cazorla, A., Lyamani, H., Denjean, C., Fuertes, D., Pérez-Ramirez, D., Torres, B., Toledano, C., Dubovik, O., Cachorro, V. E., Frutos, A. M., Olmo, F. J., Alados-Arboledas, L. Retrieval of aerosol profiles combining sunphotometer and ceilometer measurements in GRASP code. Atmos. Res., 204, 161, 177, 2018.

Rose, T., Creewll, S., Löhnert, U., Simmer, C.: A network suitable microwave radiometer for operational monitoring of cloudy atmosphere. Atmos. Res., 75, 3, 183 – 200, 2005.

Stull, R. B., Santoso, E., Berg, L., Hacker, J.: Boundary layer experiment 1996 (BLX96), Bull. Am. Meteorol. Soc., 78, 1149–1158, 1997.

Stull, R. B.: An Introduction to Boundary Layer Meteorology, vol. 13, *Kluwer Academic Publishers, the Netherlands*, Dordrecht/Boston/London, 1988.

Stull, R. B.: Meteorology for Scientists and Engineers, 3rd Edition, *Uni. Of British Columbia*, 2011.

Titos, G., Foyo-Moreno, I., Lyamani, H., Querol, X., Alastuey, A., and Alados-Arboledas, L.: Optical properties and chemical composition of aerosol particles at an urban location: An estimation of the aerosol mass scattering and absorption efficiencies, J. Geophys.Res.-Atmos., 117, D04206, doi:10.1029/2011JD016671, 2012.

Turner, D. D., Ferrare, R. A., Wulfmeyer, V., and Scarino, A. J.: Aircraft evaluation of ground-based Raman lidar water vapor turbulence profiles in convective mixed layers, J. Atmos. Oceanic Technol., 31, 1078–1088, doi:10.1175/JTECH-D-13-00075-1, 2014

van Ulden, A. P., and Wieringa, J. :Atmospheric boundary layer research at Cabauw, Bound-Lay. Meteorol., 78,39–69, 1996.

Valenzuela, A., Olmo, F.J.ab, Lyamani, H.ab, Granados-Muñoz, M.J.ab, Antón, M.c, Guerrero-Rascado, J.L.ab, Quirantes, A.a, Toledano, C.d, Perez-Ramírez, D.ef, Alados-Arboledas, L.: Aerosol transport over the western mediterranean basin: Evidence of the contribution of fine particles to desert dust plumes over alborán island. J. Geophys Res., 119, 24, 14,028-14,044, 2014.

Vogelmann, A. M., McFarquhar, G. M., Ogren, J. A., Turner, D. D., Comstock, J. M., Feingold, G., Long, C. N., Jonsson, H. H., Bucholtz, A., Collins, D. R., Diskin, G. S., Gerber, H., Lawson, R. P., Woods, R. K., Andrews, E., Yang, H., Chiu, J. C., Hartsock, D., Hubbe, J. M., Lo, C., Marshak, A., Monroe, J. W., Mcfarlane, S. A., Jason, M., and Toto, T.: RACORO extended-term aircraft observations of boundary layer clouds, Bull. Am. Meteorol. Soc., 93, 861–878, doi:10.1175/BAMS-D-11-00189.1, 2012.

Williams, A. G., and Hacker, J. M.: The composite shape and structure of coherent eddies in the convective boundary layer, Bound-Lay. Meteorol., 61, 213–245, 1992.

Wulfmeyer, V.: Investigation of turbulent processes in the lower troposphere with water vapor DIAL and radar-RASS, J. Appl. Sci., 56, 1055–1076, 1999.

Wulfmeyer, V., Pal., S., Turner, D. D., and Wagner, E.: Can water vapour Raman lidar resolve profiles of turbulent variables in the convective boundary layer?, Bound-Lay. Meteorol., 136, 253–284, doi:10.1007/s10546-010-9494-z, 2010.

Table 1 – Variables applied to statistical analysis (Lenschow et al., 2000)

	Without Correction	Correction	Error
Integral Time Scale (τ)	$\int_{0}^{\infty} q'(t)dt$	$\frac{1}{\overline{q'^2}} \int_{t\to 0}^{\infty} M_{11}(t)dt$	$\tau.\sqrt{\frac{4\Delta M_{11}}{M_{11}(\to 0)}}$
Variance ($\sigma^2_{q'}$)	$\frac{1}{T}\sum_{t=1}^{T}(q(t) - \overline{q})^2$	$M_{11}(\to 0)$	$q^2.\sqrt{\frac{4\Delta M_{11}}{M_{11}(\to 0)}}$
Skewness (S)	$\frac{\overline{q^3}}{\sigma_q^3}$	$\frac{M_{21}(\to 0)}{M_{11}^{3/2}(\to 0)}$	$\frac{\Delta M_{21}}{\Delta M_{11}^{3/2}}$
Kurtosis (K)	$\frac{\overline{q^4}}{\sigma_q^4}$	$\frac{3M_{22}(\to 0) - 2M_{31}(\to 0) - 3\Delta M_{11}^2}{M_{11}^2(\to 0)}$	$\frac{4\Delta M_{31} - 3\Delta M_{22} - \Delta M_{11}^2}{\Delta M_{11}^2}$

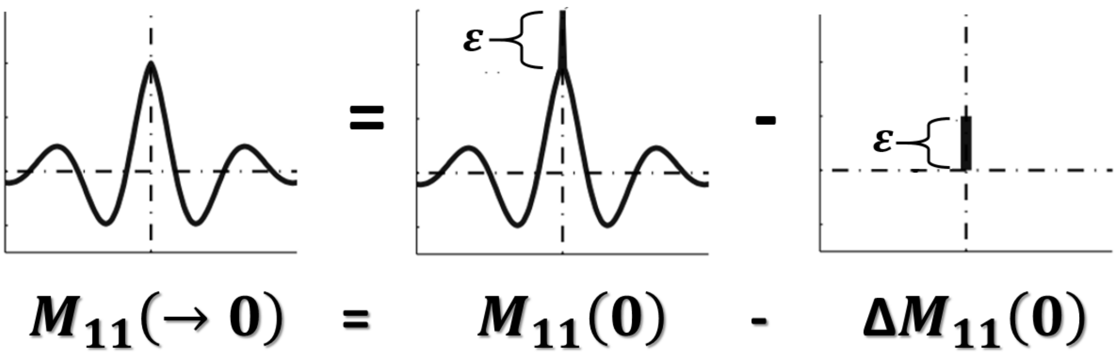

Figure 1 – Procedure to remove the errors of autocovariance functions. $M_{11}(\to 0)$ – corrected autocovariance function errors; $M_{11}(0)$ - autocovariance function without correction; $\Delta M_{11}(0)$ - error of autocovariance function

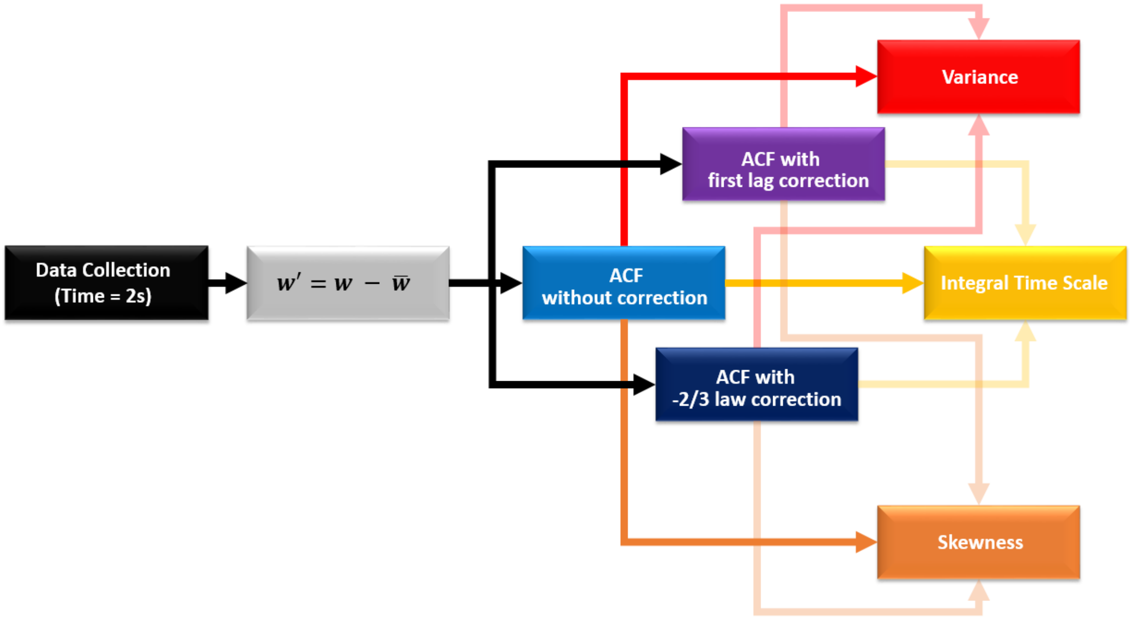

Figure 2 – Flowchart of data analysis methodology applied to the study of turbulence with Doppler lidar

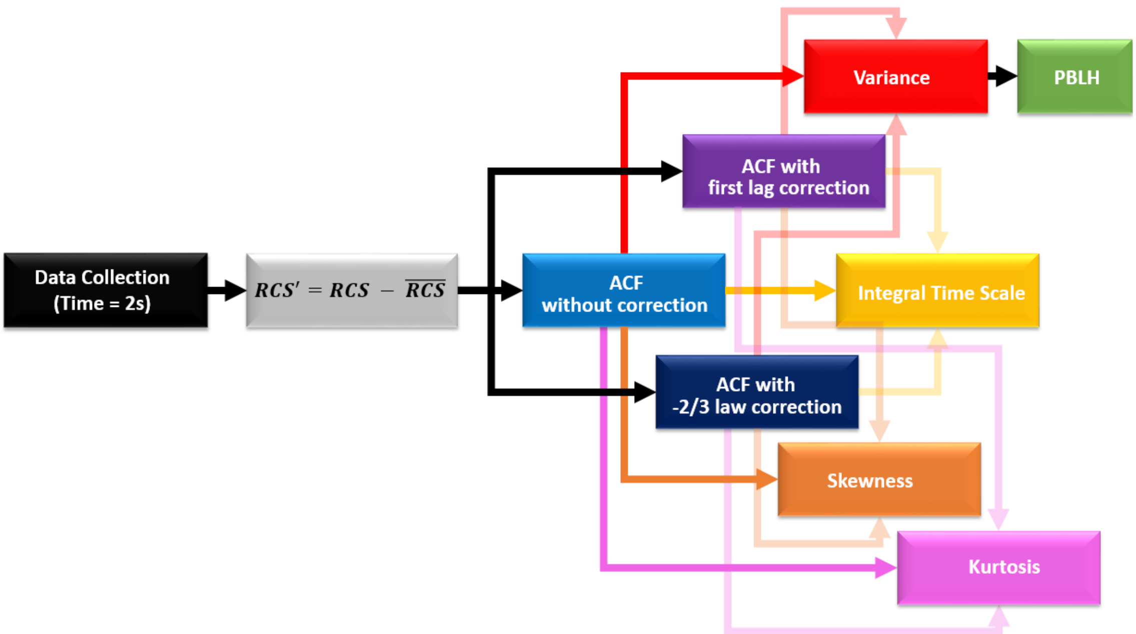

Figure 3 – Flowchart of data analysis methodology applied to the study of turbulence with elastic lidar

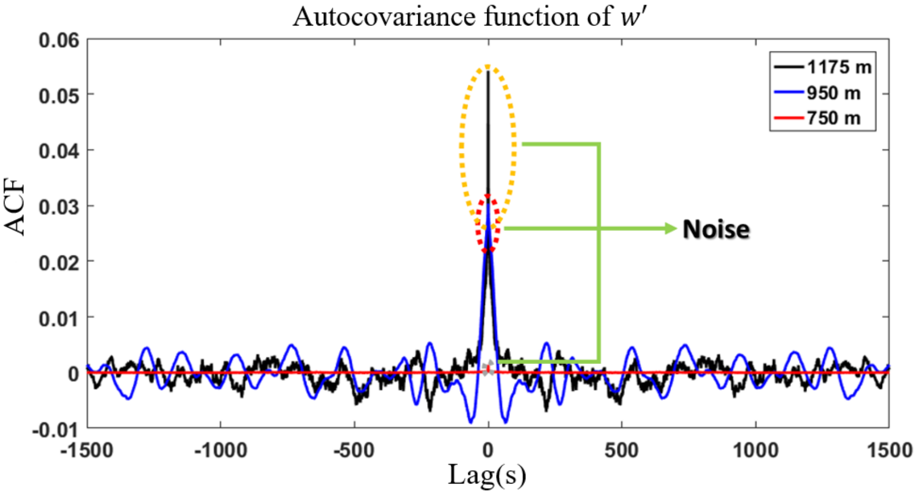

Figure 4 – Autocovariance function (ACF) of w' at three different heights

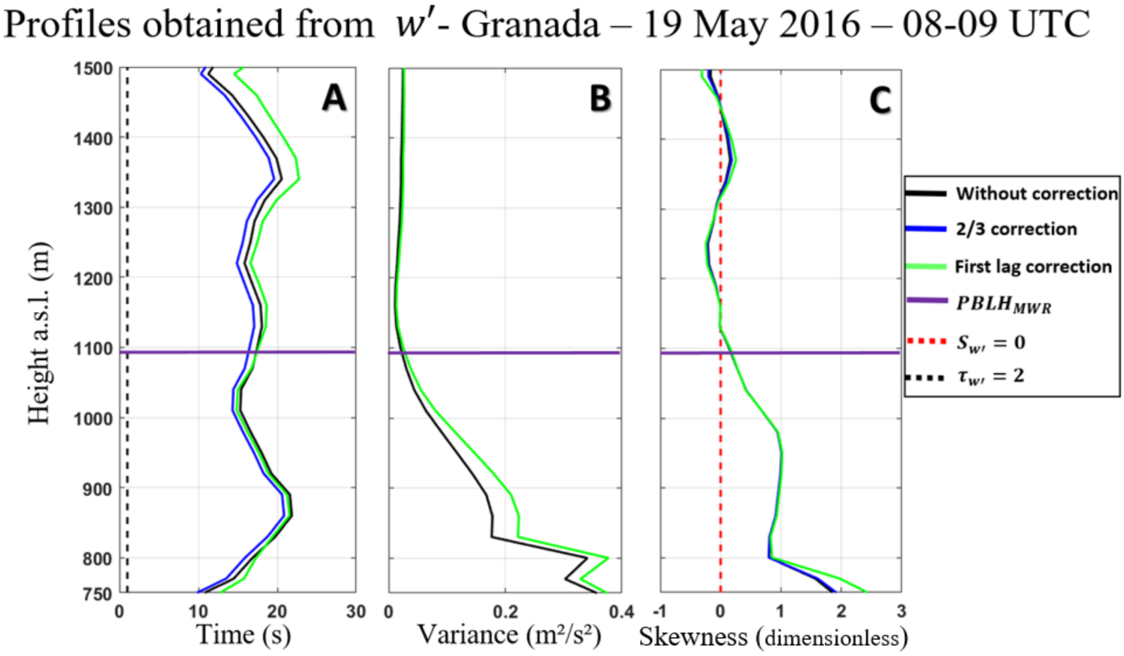

Figure 5 – A - Vertical profile of Integral time scale ($\boldsymbol{\tau_{w'}}$). B - Vertical profile of variance ($\boldsymbol{\sigma^2_{w'}}$). C - Vertical profile of Skewness. ($\boldsymbol{S_{w'}}$)

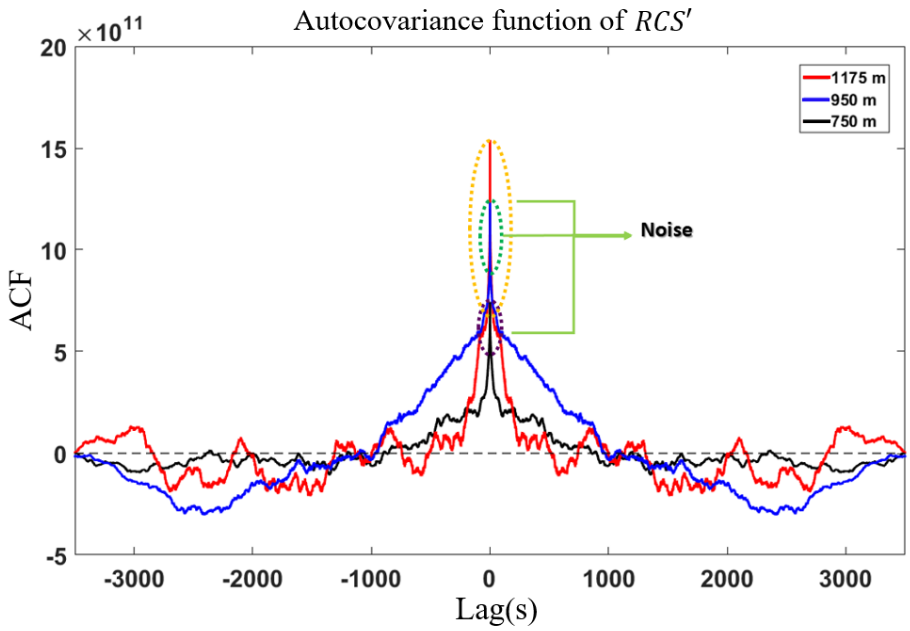

Figure 6 – Autocovariance of RCS' to three different heights

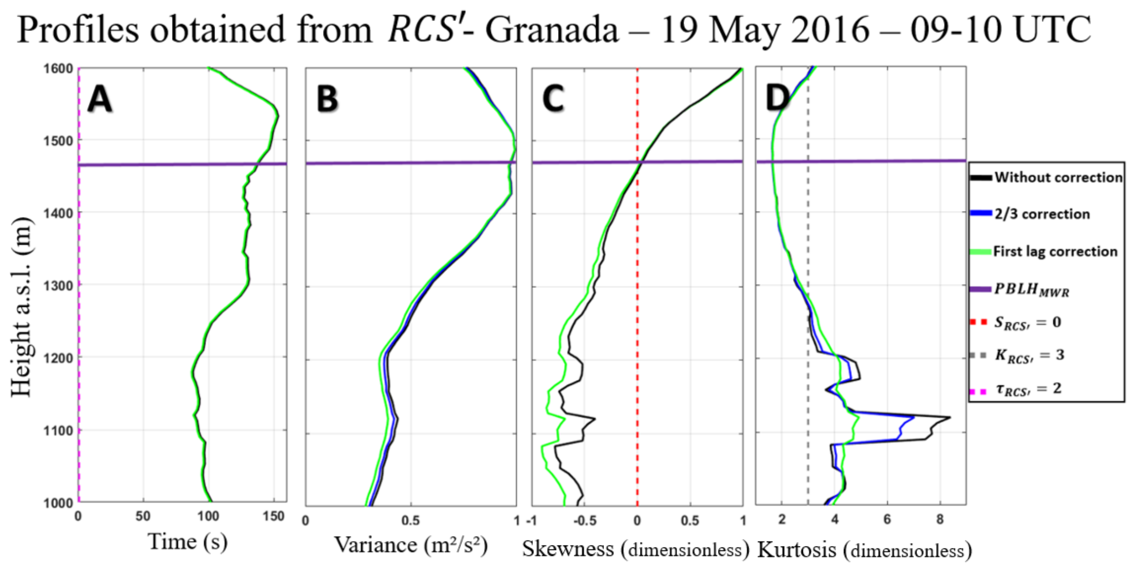

Figure 7 – A- Vertical profile of Integral time scale ($\boldsymbol{\tau_{RCS'}}$). B - Vertical profile of variance ($\boldsymbol{\sigma^2_{RCS'}}$). C - Vertical profile of Skewness ($\boldsymbol{S_{RCS'}}$). D - Vertical profile of Kurtosis ($\boldsymbol{K_{RCS'}}$).

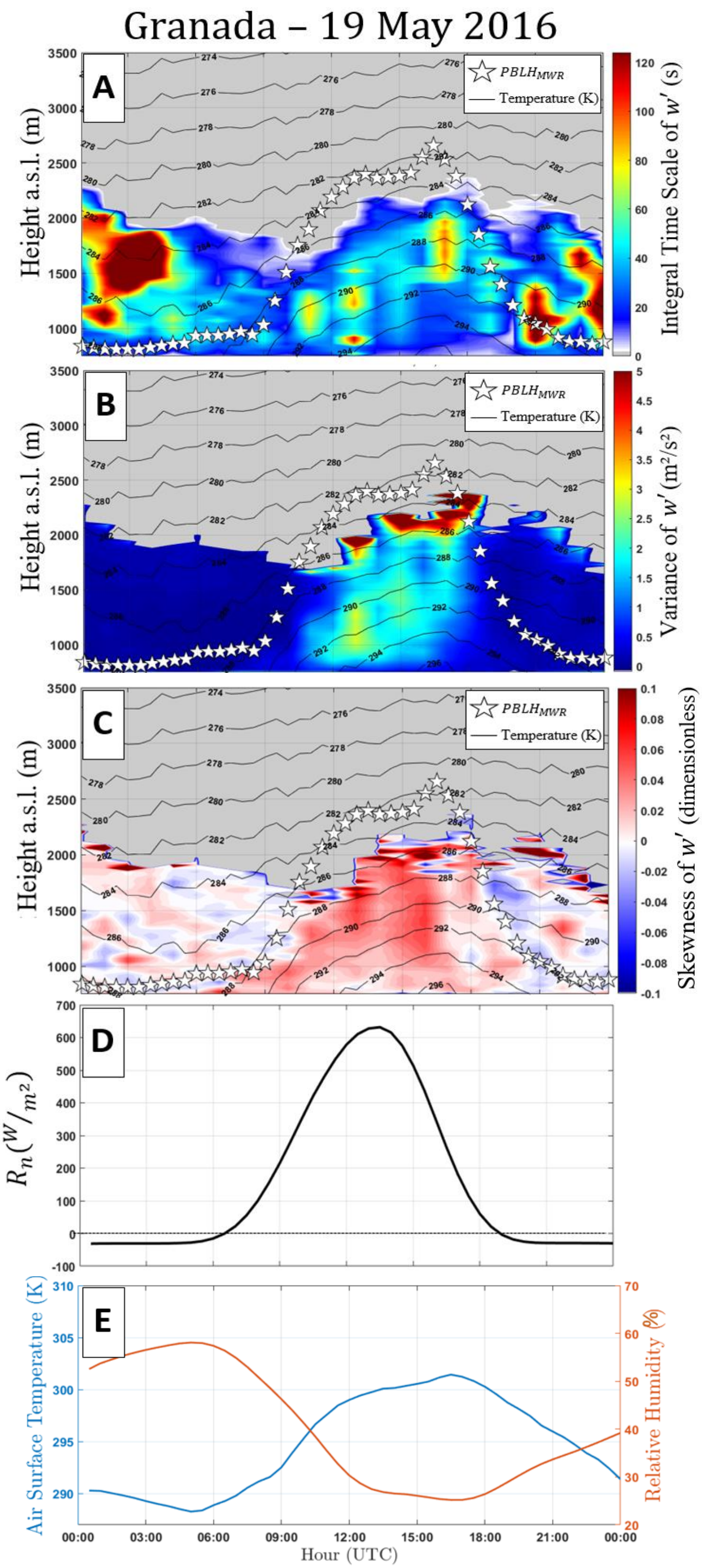

Figure 8 – A – integral time scale [$\boldsymbol{\tau_{w'}}$], B – variance [$\boldsymbol{\sigma^2_{w'}}$], C – skewness [$\boldsymbol{S_{w'}}$], D – net radiation [$R_n$], E – Air surface temperature [blue line] and surface relative humidity [RH – orange line]. In A, B and C black lines and white stars represent air temperature and $PBLH_{MWR}$, respectively.

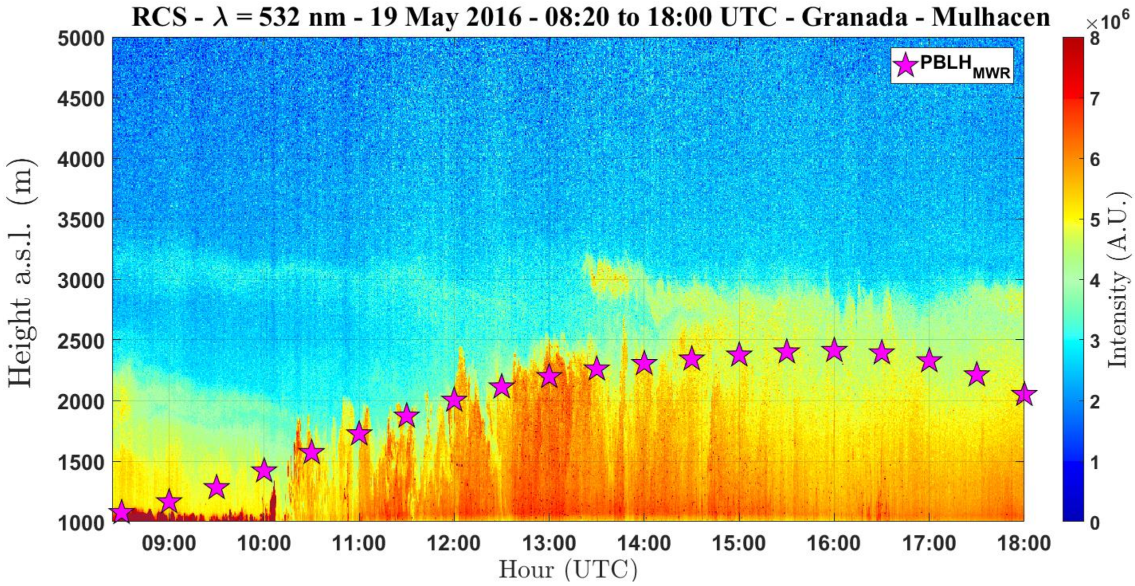

Figure 9 – Time-Height plot of RCS - 19 May 2016. Pink stars represent $PBLH_{MWR}$

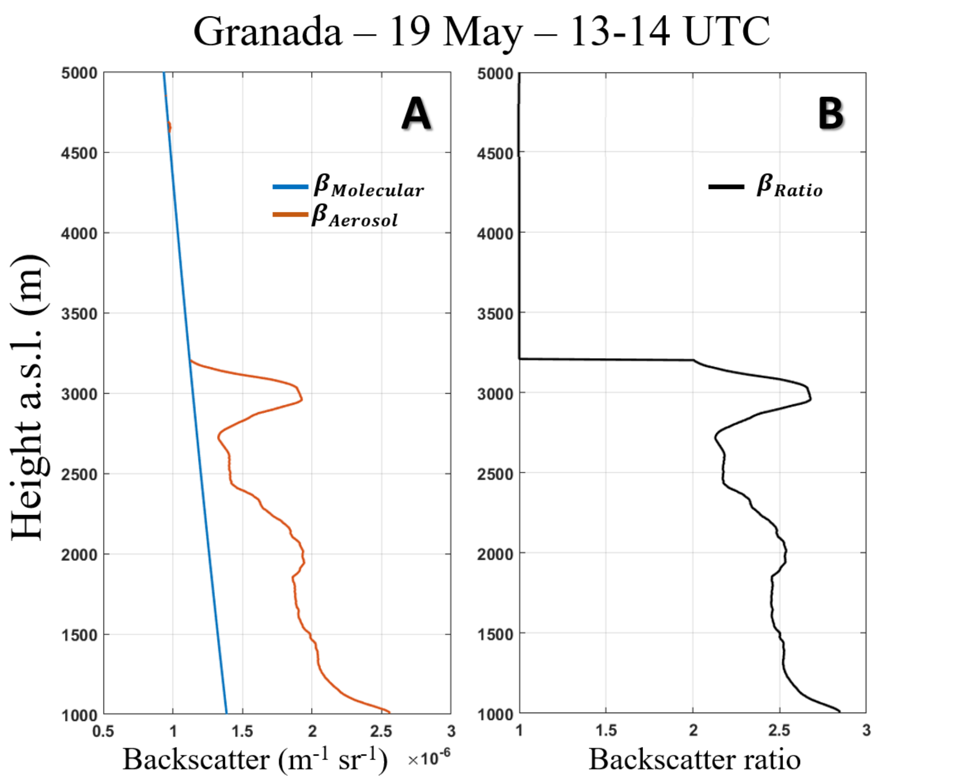

Figure 10 – (A) $\beta_{Molecular}$ (blue line) and $\beta_{Aerosol}$ (orange line). (B) β_{Ratio} (black line). All profiles were obtained from the 532 nm lidar signal

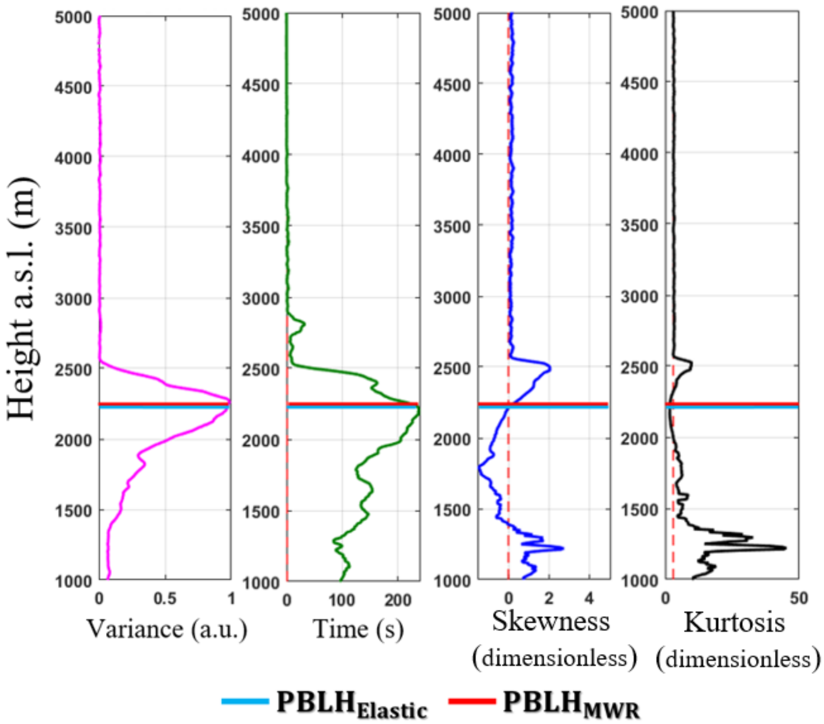

Figure 11 – Statistical moments obtained from elastic lidar data at 13 to 14 UTC - 19 May 2016. From left to right: variance [$\boldsymbol{\sigma}^2_{RCS'}$], integral time scale [$\boldsymbol{\tau_{RCS'}}$], skewness [$\boldsymbol{S_{RCS'}}$] and kurtosis [$\boldsymbol{K_{RCS'}}$].

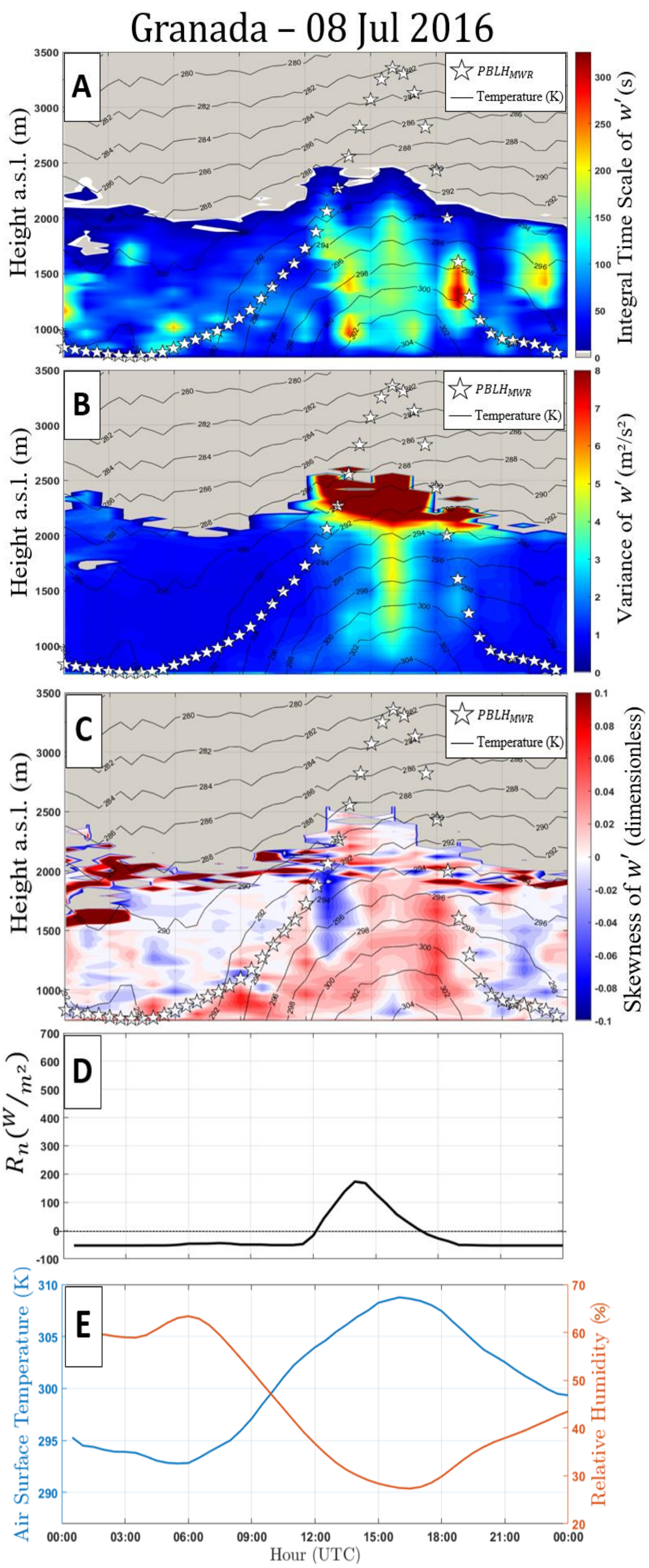

Figure 12 - A – integral time scale [$\boldsymbol{\tau_{w'}}$], B – variance [$\boldsymbol{\sigma^2_{w'}}$], C – skewness [$\boldsymbol{S_{w'}}$], D – net radiation [$R_n$], E – Air surface temperature [blue line] and surface relative humidity [RH – orange line]. In A, B and C black lines and white stars represent air temperature and $PBLH_{MWR}$, respectively.

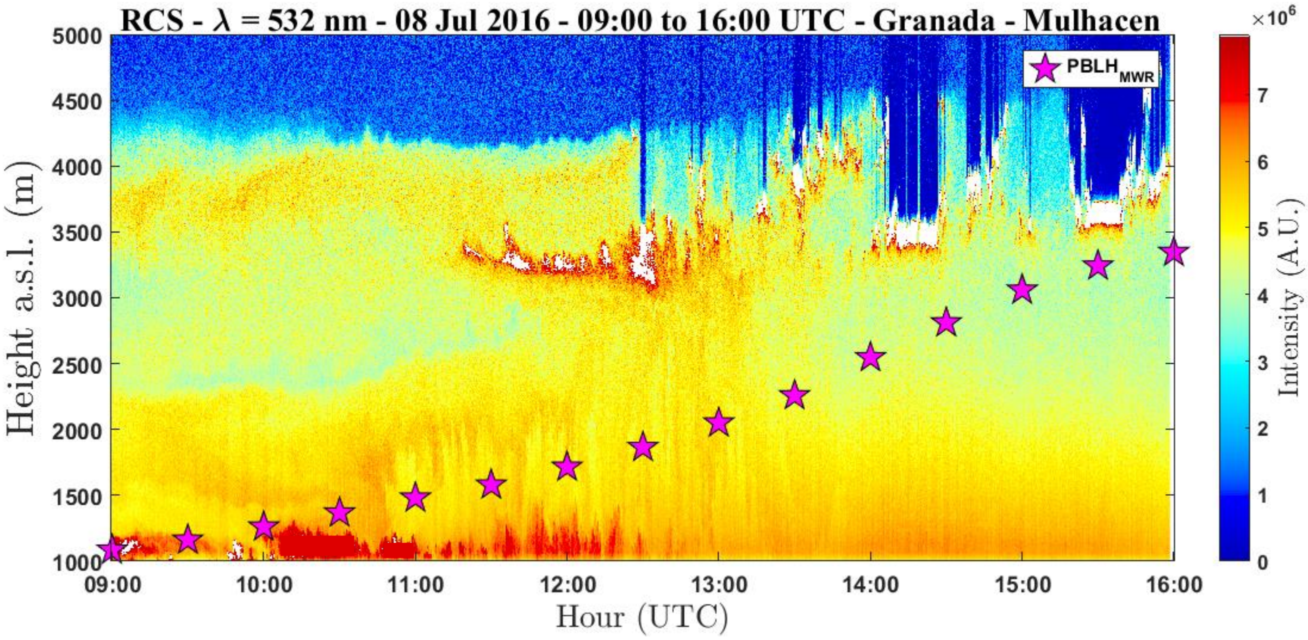

Figure 13 – Time-Height plot of RCS - 08 July 2016. Pink stars represent $PBLH_{MWR}$.

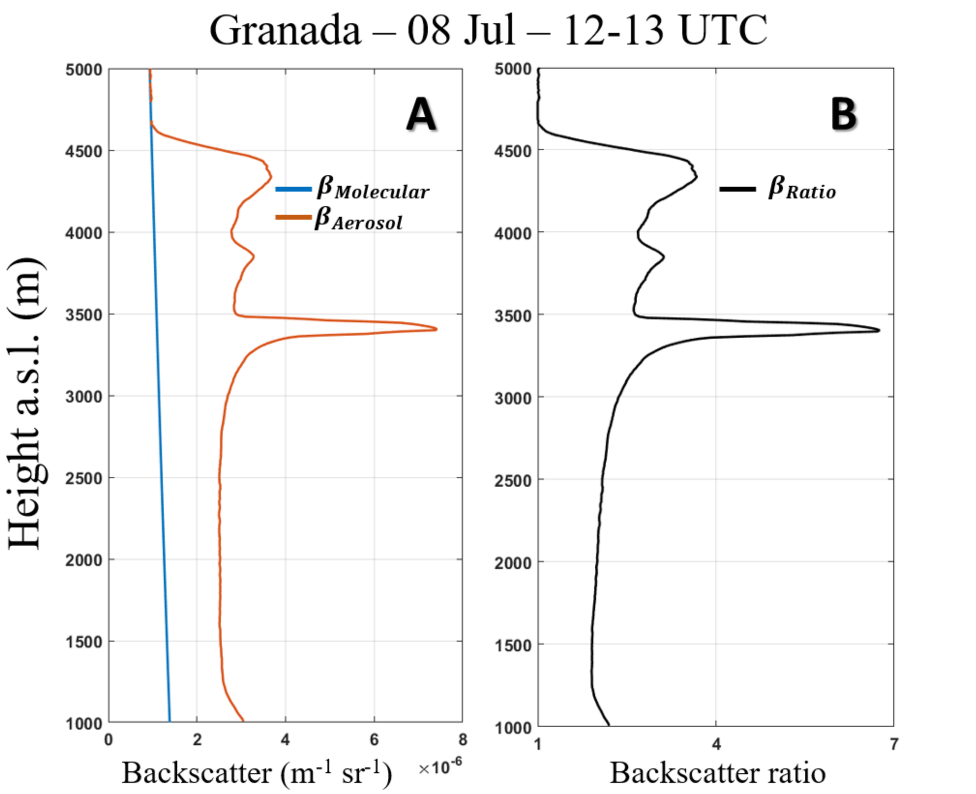

Figure 14 – (A) $\beta_{Molecular}$ (blue line) and $\beta_{Aerosol}$ (orange line). (B) β_{Ratio} (black line). All profiles were obtained from the 532 nm lidar signal

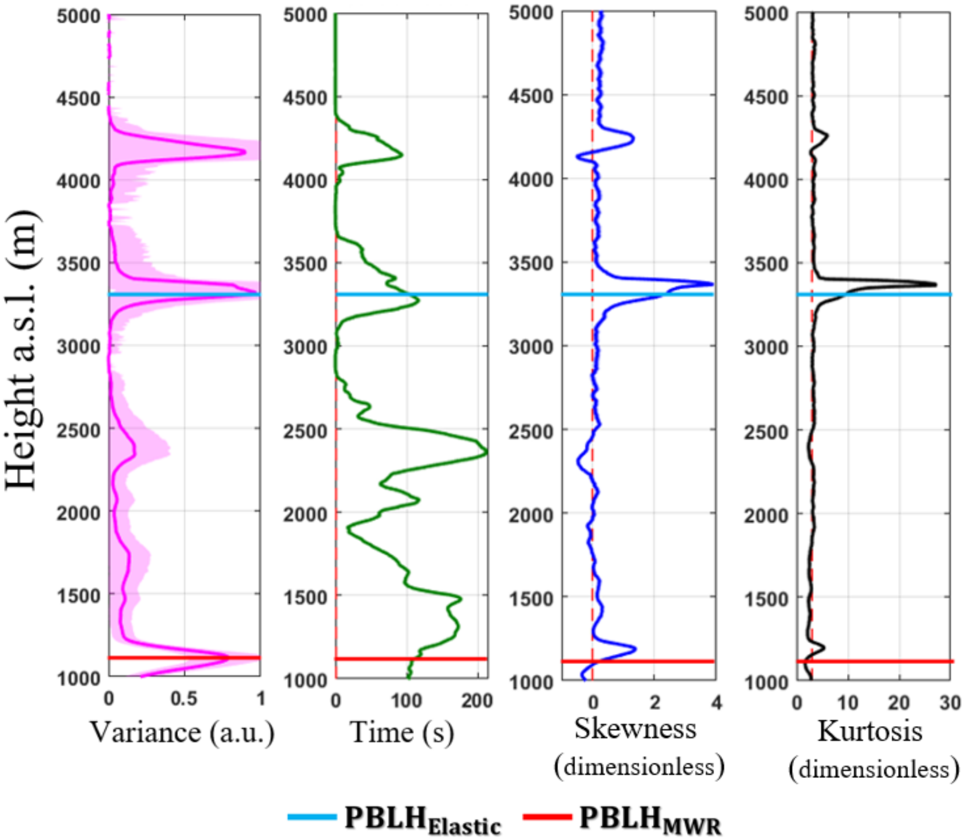

Figure 15 - Statistical moments obtained from elastic lidar data at 11 to 12 UTC - 08 July 2016. From left to right: variance [$\boldsymbol{\sigma}^2_{RCS'}$], integral time scale [$\boldsymbol{\tau}_{RCS'}$], skewness [$\boldsymbol{S}_{RCS'}$] and kurtosis [$\boldsymbol{K}_{RCS'}$].

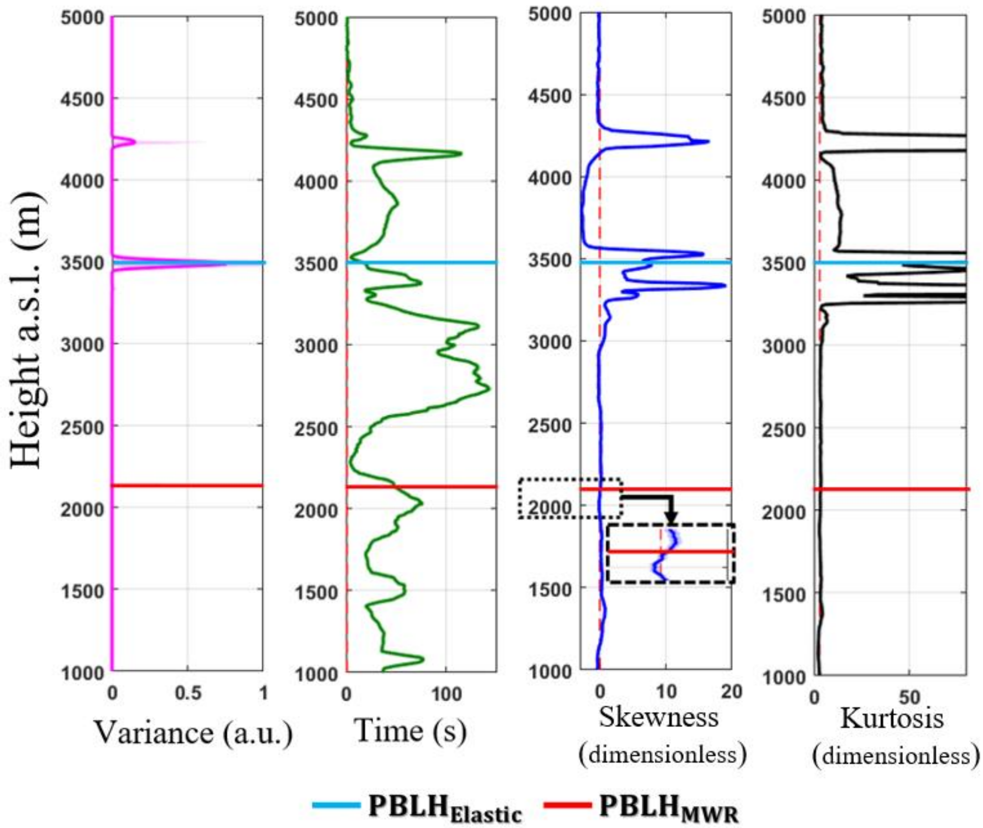

Figure 16 - Statistical moments obtained from elastic lidar data at 12 to 13 UTC - 08 July 2016. From left to right: variance [$\boldsymbol{\sigma}^2_{RCS'}$], integral time scale [$\boldsymbol{\tau}_{RCS'}$], skewness [$\boldsymbol{S}_{RCS'}$] and kurtosis [$\boldsymbol{K}_{RCS'}$].